Exploring the Intricacies behind Dark Matter Direct Detection Machines

Sanjana Mittal

Dubai College, Dubai, UAE

Abstract: From the 19th century hypotheses of Lord Kelvin, to the later conjectures of Poincare and Zwicky, the existence of dark bodies or '"matière obscure" has long been posited. Dark matter was established as a fundamental unsolved problem in the fields of particle physics and astronomy after the influential evaluation of galaxy rotation curves by Rubin and Ford in the 1970s, and since then, the scientific community has made much progress to uncover the elusive secrets of dark matter. This paper first introduces the fundamental features and hypothesised characteristics of dark matter and delineates key scientific evidence pointing to its existence. It then moves onto a detailed exploration of dark matter direct direction machines: their function and principles, derivations of key mathematical quantities used, manipulation of these quantities using computational methods, the application of these methods to the LUX liquid Xenon experiment and the CDMS cryogenic Germanium experiment, and an overview of the engineering of key components and detectors used in such highly sensitive experiments.

1.1 WHAT IS DARK MATTER?

The term dark matter refers to a hypothesized form of matter that does not interact electromagnetically with other particles from the Standard Model, and is posited to comprise up to 85% of the matter in the known observable universe. Dark matter is thought to consist of undiscovered subatomic particles that do have a distinct mass and thus generate gravity, but do not interact with the electromagnetic force and hence do not absorb, emit or reflect light. This quality has made it extremely difficult to study or understand dark matter, and while most of the scientific community agrees upon its existence, many have postulated differing models such as modified Newtonian Dynamics or entropic gravity instead (Angus et. al., 2013)

1.2 EVIDENCE

There are a variety of astrophysical observations that imply the existence of dark matter.

1.2.1 MASS DISTRIBUTIONS

One of the most prominent avenues of evidence, is the notion that galaxies are bound by more gravity than their observable masses can possibly generate, and that without the existence of some additional source of gravity (i.e dark matter) they would fly apart.

The mass distributions of all systems are considered to be similar to that of the Solar System, in that only a negligible percentage of the system's total mass comes from non-luminous sources. Hence the mass of a galaxy or system inferred from the brightness of its luminous matter should match its gravitational mass. However, when gravitational mass is calculated using the virial theorem, which relates a systems average kinetic energy to its total potential energy, this mass does not match the mass calculated from the galaxy's luminous matter. The mass required to generate the gravity holding galaxies and systems together is much greater than the mass of their luminous matter, hence there must be some large amount of nonluminous matter that accounts for this discrepancy.

1.2.2 GALAXY ROTATION CURVES

Galaxy rotation curves also point to the existence of some powerful source of matter that is currently not known. The rotation curve of a galaxy is a plot of the orbital speeds of visible stars in the galaxy, against their radial distance from the galaxy's center. According to Newton's Law of Gravitation and Kepler's Third Law, rotational velocity of a satellite (a star) should be roughly inversely proportional to its distance from the galactic center, as per the virial theorem below:

$$v = \sqrt{\frac{GM}{r}},$$

where v is the velocity of the satellite, G is the gravitational constant, M is the mass, and r is the radius from the center of the galaxy. Smaller systems whose mass is concentrated in their center (i.e. systems consisting of stars and planets, or

planets and moons) do obey this principle, and in the Solar System for example, planets closer to the Sun have a greater orbital speed than those that are further away.

However, when galaxy rotation curves are plotted, it is invariably found that a 'flat' graph is produced. Rotational velocities of stars plateau despite an increasing distance from the galactic center of gravity.
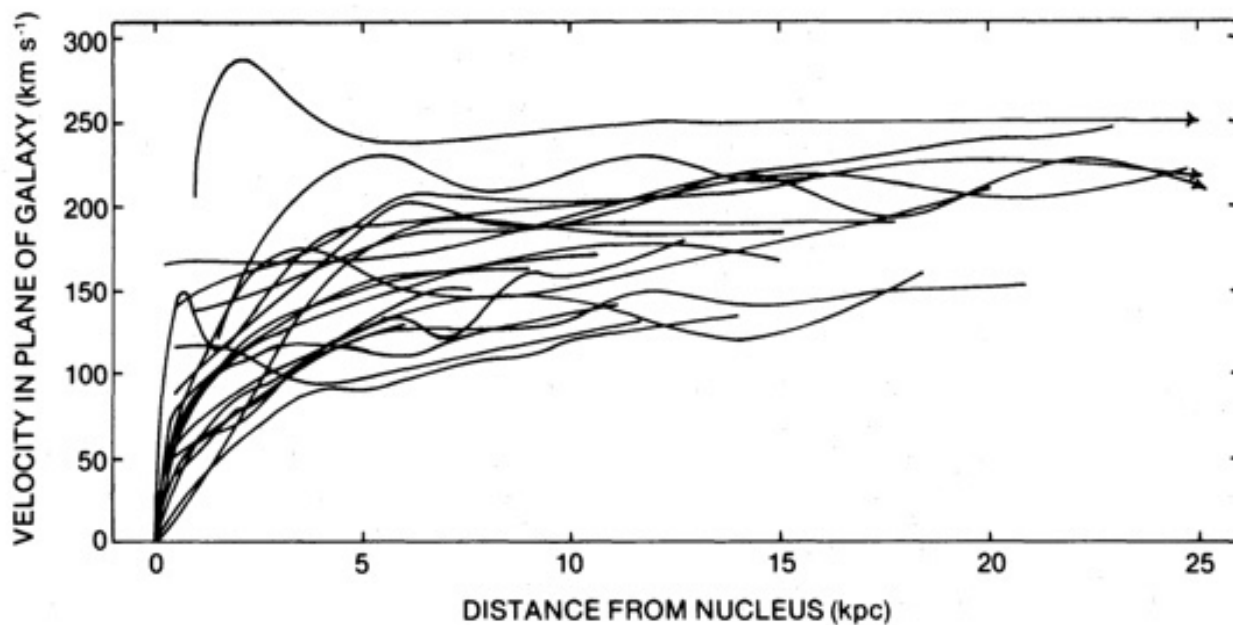

Fig. 1. Rotation curves of spiral galaxies (Rubin et. al., 1978). Most galaxies show an unexpected flattening of the circular velocity at large radial distances.

This counterintuitive result suggests that mass distributions within galaxies on a large scale cannot be modeled the same way it is for smaller systems, and that mass within a galaxy is derived from areas other than the galactic center – from dark matter. It has been postulated and generally accepted, that the dark matter would have to be located in a massive, roughly spherical halo enshrouding each galaxy.

Fig. 2. Two views from Hubble of the massive galaxy cluster Cl 0024+17 (ZwCl 0024+1652) from NASA, ESA, M.J. Jee and H. Ford (Johns Hopkins University)

1.2.3 GRAVITATIONAL LENSING

Another observation that evidences dark matter is gravitational lensing. General relativity states that large masses warp and curve space time, and hence a massive object will act as a lens to bend light coming to an observer from a more distant source. By observing the areas around massive clusters of galaxies, one can reverse-engineer the distortions of the consequent warped background galaxy images and determine where the densest concentrations of matter lie. Mathematical models allow astronomers to determine the location and properties of the matter that acting as a lens, and these models show that the lensing observed is attributed to far greater masses than what is observable; there must be a significant nonluminous source of mass to cause this gravitational lensing.

1.2.4 COSMIC MICROWAVE BACKGROUND RADIATION

Another factor supporting the theory of dark matter is the imprints found in Cosmic Microwave Background radiation (CMB). CMB is the result of the high energy electromagnetic waves released during the Big Bang cooling into low energy background radiation over time. The patterns that we see in CMB are caused by the force of gravity causing matter to fall inwards, and pressure exerted by photons causing matter to expand outwards. These competing forces are responsible for the oscillation of photons and matter into and out of dense regions of CMB that we see today. Dark matter does not interact directly with this radiation, but it does affect CMB by its gravitational potential. Ordinary matter perturbations are affected by both the inward pull of gravity and the outward pressure of photons, however dark matter perturbations are affected only by the inward pull of gravity and are unaffected by any outwards forces caused by photons. This means that dark matter collects in regions of high density and exacerbates the gravitational collapse of matter, thus leaving a characteristic imprint on CMB observations that is difficult to explain otherwise.

2.1 DARK MATTER DETECTION

As mentioned earlier, dark matter is hypothesized to be made up of an undiscovered type of subatomic particle. The search then, is to find this particle. If this hypothesis is assumed to be correct, then, similar to neutrinos, millions of such particles must pass through every square centimeter of the universe (and Earth) each second. Weakly Interacting Massive Particles (WIMPs) are a popular candidate particle with mass ranges of 2GeV - 100TeV (Roszkowski et. al., 2018), alongside the axion, a less massive particle with mass ranges of 0.05 and 1.50 meV (Borsanyi et. al., 2016), which is also gaining traction. Experiments to detect any hypothesized candidate particles fall into two main categories: indirect detection, and direct detection.

2.1.1 INDIRECT DETECTION

Indirect detection experiments search for the products of the self-annihilation or decay of dark matter particles in outer space. Dark matter particles could collide in space to produce gamma rays or Standard Model particle-antiparticle pairs, or even Standard Model particles if the dark matter particle is unstable. These processes could be detected indirectly through an excess of gamma rays, antiprotons or positrons emanating from high density regions in our galaxy or others. However, indirect detection is a difficult task because various astrophysical sources can mimic the signals expected from dark matter, so a conclusive discovery is rendered unlikely.

2.1.2 DIRECT DETECTION

Direct detection experiments search for a dark matter particle itself on Earth. They aim to observe extremely low-energy recoils of nuclei induced by interaction with dark matter particles passing through Earth. After such a recoil, the nucleus will emit energy the form of scintillation, which can be detected by apparatus, and hence signify a dark matter particle interaction. Low background interference is crucial for such experiments and hence most operate in deep underground facilities to filter out interference from background radiation. Direct detection experiments can be further categorized into cryogenic, or noble liquid detectors. Cryogenic detectors operate at extremely low temperatures and detect the heat produced when a particle hits an atom in a crystal absorber (e.g. germanium). Noble liquid detectors detect scintillation produced by a collision in a liquidized noble gas such as argon or xenon. Both techniques' success is determined by their ability to distinguish between background particles scattering off of electrons, and dark matter particles scattering off of nuclei.

3.1 THE LARGE UNDERGROUND XENON EXPERIMENT

The Large Underground Xenon experiment (LUX) was a large-scale collaboration that aimed to search for the WIMP dark matter particle candidate by constructing a dual-phase liquid-xenon direct detection machine. The LUX detector aimed to detect WIMPs with a spin independent cross-section of per nucleon, which evaluates to approximately 1 scattering event per 100kg per month in the inner 100kg fiducial volume of liquid xenon within the total 370kg detector. Like most other direct detection endeavors, it was crucial for the LUX detector to be able to identify and exclude background interaction events (electron recoils from gamma rays and nuclear recoils from electrons) and ensure that during a 10-months running period, not a single WIMP candidate detected

in the fiducial volume is due to background interactions. (Akerib et. al., 2012)

3.2 STRUCTURE

The LUX detector consists of two cryostat vessels made thick grade CP1 titanium sheets. The outer cryostat vessel holds a vacuum to insulate the inner vessel while the inner vessel contains the detector internals, the time projection chamber and the liquid xenon. The inner vessel is a cylinder with a dome welded to the bottom and a flange welded to the upper rim. It hangs from the upper dome of the outer vessel and is mechanically attached and thermally isolated. Instrumentation, wiring and circulation plumbing lines penetrate through the outer vessel into the inner vessel and the flanges of both vessels are designed to use Helicoflex gaskets.
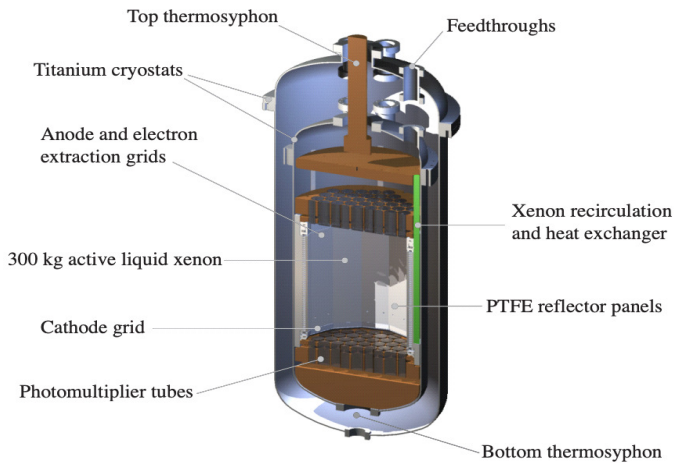

Fig. 3. A detailed cross-sectional view of the LUX cryostats. (Akerib et. al., 2012)

3.2.1 TIME PROJECTION CHAMBER AND DETECTION PROCESS

The LUX time projection chamber (TPC), located in the inner cryostat vessel, is essentially the heart of the experiment and is the mechanism by which particle interactions are detected. In general, a time projection chamber is a type of particle detector that uses a combination of electric fields and magnetic fields, alongside a sensitive volume of gas or liquid, to perform a 3-D reconstruction of a particle trajectory or interaction. In a basic TPC, charged particles traverse a gas/liquid volume and ionize atoms of the gas along their trajectories. A high electric field is then applied between the endplates of the chamber, and so the released electrons (as a result of the ionization of fluid nucleons) drift in this field towards the anode endplate of the chamber. To then be able to measure the position of the particle trajectory as accurately as possible, the homogeneity of the electric field is crucial. This is often achieved by a field cage, which usually consists of

conducting rings around the cylinder. These rings divide the potential from the cathode stepwise down to the anode.

Two-phase liquid xenon detectors, such as the one employed in the LUX collaboration, use slightly differing technology for the detection of dark matter, while still following the basic principles of detecting scintillation and using an electric field to drift electrons as a means of dark matter direct detection.

As depicted in Figure 4, scattering events between possible WIMPs and the target liquid xenon nucleons create direct scintillation light, while ionization electrons escaping at the event site are drifted upwards (by applied electric fields between a cathode grid at the bottom of the TPC and an anode grid at the top of the TPC) to the liquid surface and extracted into the gas phase, where they create electro-luminescence light signals. Both of these signals are measured by arrays of sensitive photomultiplier detectors (PMTs), located above and below the active liquid xenon region. The bottom PMT array measures the first scintillation signal, as photons in the liquid are mostly trapped by total internal reflection. The top PMT array detects and images the x/y location of the second electro-luminescence signal, and thus the x/y location of the scattering event site. The drift time, obtained from the time difference between the first and second signals, gives the depth of the interaction. In this way, the technique provides 3D imaging of the event location.
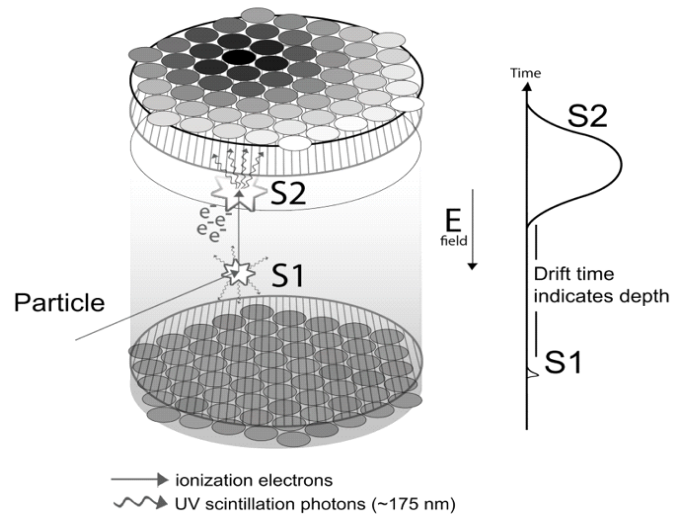

Fig. 4. Schematic of a dark matter interaction in a two-phase xenon detector. The primary scattering interaction in the liquid xenon produces scintillation light (S1). The ionization electrons created during the primary interaction, create an electroluminescence pulse (S2) after entering the gas region above the liquid. The S1 and S2 light is captured with two arrays of PMTs, located below and above the active region of the detector. (Akerib et. al., 2012)

Liquid xenon is used because it is a noble gas that has no naturally occurring radioactive isotopes, and can be readily purified, providing very low internal radioactivity. External background interactions are minimized by the choice of detector materials and the design of shielding. Further elimination of background interactions is achieved by determining and excluding electron recoils and nuclear recoils based on the ratio of charge to scintillation light and precise 3D event position imaging.

The LUX time projection chamber is a dodecagonal structure enclosing an active region which contains approximately 300 kg of liquid xenon and arrays of 61 PMTs each, above and below.
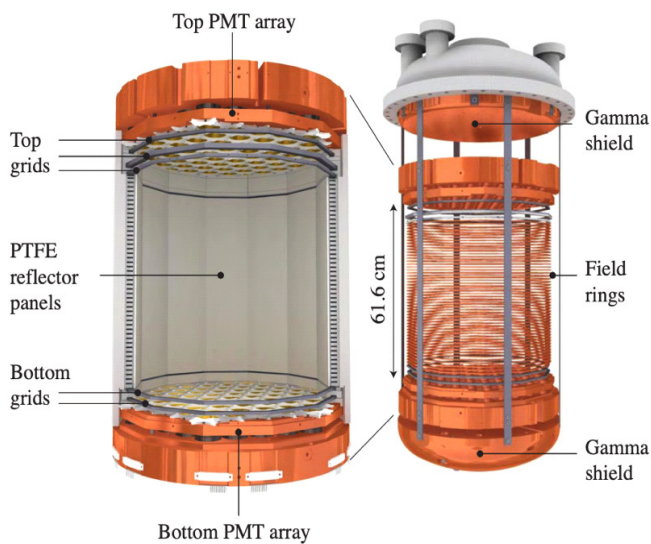

Fig. 5. Rendering of the LUX TPC, supported from the top flange of the inner cryostat.

The inner walls of the TPC consist of twelve polytetrafluoroethylene (PTFE) reflector panels that cover forty-eight copper field rings. The copper field rings form a field cage to ensure homogeneity of the electric field created, and divide the potential from the cathode endplate stepwise down to the anode endplate. The LUX TPC supplies 100 kV to the cathode grid in order to create a 2 kV/cm drift field in the liquid. However, this presents numerous challenges, as high-purity noble gases discharge very readily. The LUX cathode high-voltage system places the feedthrough outside the external water shield, which forms a vacuum seal between a commercial high-voltage cable and a standard con-flat flange. This system avoids discharges in the xenon by excluding gas from all high-field regions.

The TPC field cage also includes five grids, supported by PTFE structures, that maximize light collection and minimize the leakage of scintillation light from xenon outside the TPC

into the viewing region, thus improving accuracy of signal detections obtained from the PMTs.

The entire structure is supported from the top flange of the inner vessel and a thick copper disk is mounted directly on to the flange. It connects to the large capacity thermosyphon through a cold finger and is used for temperature control, heat sinking of cables, and serves as a γ shield. All other components are supported from six titanium straps attached to this shield. Below the bottom PMT support, a thick copper structure fills the dome shape of the inner vessel to displace inactive xenon and to provide additional γ shielding. This copper structure is also connected to a thermosyphon to provide further control of the temperature gradient in the detector and to adjust the temperature of the returning xenon as it is circulated within the circulation system.

3.2.2 PMTS AND LIGHT COLLECTION

As mentioned earlier, the LUX detector uses two arrays of 61 PMTs. The array is placed above the liquid surface (on the top of the TPC near the anode grid) is used to determine x/y positions of scattering interaction events from the secondary electro-luminescence signal pattern. These PMTs achieve a position accuracy of ~1 cm using similar likelihood pattern recognition techniques as used on earlier detectors such as XENON10 and ZEPLIN. The second array is placed in the liquid, below the cathode grid. This array gets most of the primary scintillation signal, due to most photoelectrons undergoing total internal reflection at the liquid surface.
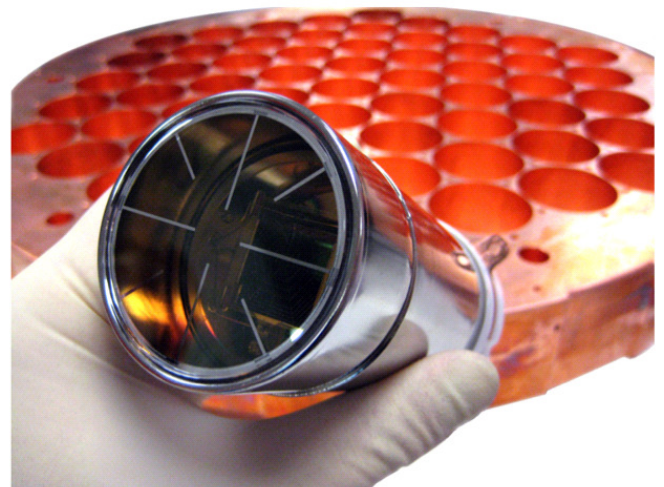

Fig. 6. A Hamamatsu R8778 PMT used in the LUX detector and one of the supporting copper blocks (Akerib et. al., 2012).

Even the electric field grids have been designed to minimize optical effects and their interference with the signals detected by the PMTs. The grids are 96-99% transparent at 0∘ angle of

incidence, due to thin wire diameter, large spacing, and the use of a strung pattern instead of a mesh. The exception is the anode grid, which uses a mesh design and is 88% transparent. The grids are constructed from stainless steel, a material shown to be ~57% reflective at xenon scintillation wavelengths

An overarching slow control database is used to manage all aspects of PMT handling and characterization, as well as all other instrumentation such as thermometers, level gauges, high-voltage systems and gas analysers. All data is stored permanently in a master database both on-site and off-site, accessible through a web browser, In total more than two hundred sensors and instruments are monitored and controlled by the slow control system.

3.2.3 COOLING

The LUX detector is cooled using a cryogenic system based on thermosyphon technology. Each thermosyphon (see aforementioned structural overview and Figure 3 for reference to location of thermosyphons) consists of a sealed tube, partially filled with a variable amount of gaseous nitrogen (N_2) and is comprised of a condenser at the top, which is immersed in a bath of liquid nitrogen, an evaporator at the bottom, which is attached to the detector itself, and a passive length of stainless steel to connect the two. Each thermosyphon is closed and pressurized with N_2 gas. The N_2 condenses inside the condenser and trickles down the stainless steel length to copper evaporators. These evaporators are securely fastened to various points on the detector's inner can and so, when the condensed N_2 evaporates again, it removes heat from the detector, before rises back up to the condenser.

3.2.4 INTERNAL CIRCULATION

Furthermore, continuous purification of the xenon within the LUX detector is also paramount to maintain the required electron drift necessary for full, accurate 3D imaging. The LUX purification system removes electronegative and molecular impurities, which may have the propensity of affecting charge and light collection, using gas-phase recirculation through a commercial heated getter. As the getter requires gaseous xenon, the xenon is continuously evaporated and recondensed in the circulation system The xenon evaporates from the detector and is circulated through the getter using a double-diaphragm pump.

The dual-phase heat exchanger is used to minimize the heat-load of this process, and is instrumented with a variety of sensors for diagnostic and control functions. As the circulation rate changes, the overall liquid height in the evaporator changes. Thermometers and differential pressure measurements are used in conjunction to gauge the liquid height, as the creation of froth as a result of evaporation renders the alternative of capacitance level meters unreliable

3.2.5 WATER TANK

Moreover, the entire LUX cryostat is shielded from background radiation with a large water tank, shown below in Fig. 7. Compared to the more standard lead or polyethylene shields, a water shield blocks much more gamma ray background radiation and provides superior shielding from neutrons due to underground cavern radioactivity.
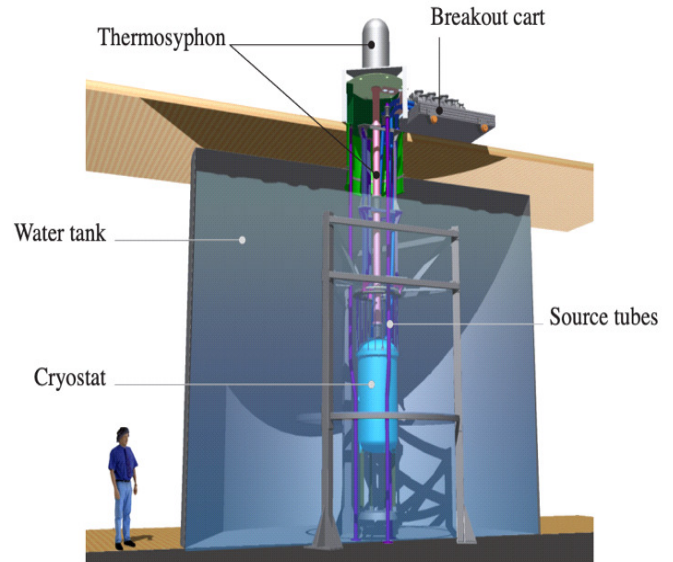

Fig. 7. Overview of the LUX detector system installed in the Davis Cavern

The water tank is also instrumented with 20 PMTs, and incoming muons (potential sources of xenon scattering interactions that must be excluded) can be tagged as they enter the water and emit Cherenkov radiation. Any nuclear recoil events in the LUX TPC's fiducial volume that are coincident with a muon in the water tank can then eliminated during data analysis and further minimize the effects of background interferences to ensure detection of WIMPs and only WIMPs.

4.1 DIRECT DETECTION RECOIL ENERGY

As this paper is focusing on direct detection methods of dark matter, and it is worthwhile to establish that when a dark matter (DM) particle collides and scatters off a nucleus of mass = m_N, the nuclear recoil energy = E_R and can be given by the following equation:

$$E_R = \frac{q^2}{2m_N},$$

where q refers to the momentum transfer of the collision and $q \sim m_\chi v$ (m_χ is the mass of a DM particle and v is its

incidentvelocity, and particles are considered nonrelativistic). Nuclear recoil is essentially just the transfer of momentum to an atomic nucleus, and hence, recoil energy is the transfer of energy associated with this transfer of momentum. This transfer of energy is emitted in the form of scintillation, and this quantity is what is detected in direct detection experiments. The equation for recoil energy above can be derived from the simple substitution of the expression for momentum, into the expression for kinetic energy, as kinetic energy is what defines the recoil energy of the collision.

$$q = mv$$

$$KE = \frac{1}{2}mv^2$$

$$KE = \frac{1}{2}\frac{(mv)^2}{m}$$

$$KE = \frac{1}{2}\frac{q^2}{m}$$

$$\therefore E_R = \frac{q^2}{2m_N}$$

This resultant equation can be used to determine the sensitivities of specific dark matter direct detection machines, as each experiment is designed to operate at particular sensitivities and search for specific DM particle masses.For example, the LUX experiment, aiming to detect WIMPs (Weakly Interacting Massive Particles), uses a medium of liquid Xenon, and so the target nucleus Xenon has a mass $m_N \sim 120\ GeV$ (Akerib et. al., 2016). This means that the sensitivity of the LUX experiment is optimal for detecting DM particles of mass $m_\chi \sim 100\ GeV$, where after substitution into q, the resultant E_R values will be aroundthe order of tens of keV – a value that is well within the limits of the detectors used in such experiments. This sensitivity therefore works well for detecting recoil energies of large DM particle candidates such as WIMPs.

4.2   SCATTERING RATES

The primary value of interest in dark matter direct detection machines, however, is the scattering rate of the dark matter particles off of the target nuclei. This quantity is given as a differential, and essentially signifies of the number of scatters per unit time, energy, and detector mass. Being able to evaluate/approximate this quantity is crucial as it provides valuable information needed to determine the viability and feasibility of an experiment, as well as the statistical significance of its results (Lisanti, 2016).

$$\frac{dR}{dE_R} = \frac{number\ of\ scatters}{time \cdot energy \cdot mass}$$

This can also be written as below:

$$\frac{dR}{dE_R} = \frac{n_x}{m_N}\left\langle v\frac{d\sigma}{dE_R}\right\rangle,$$

where n_x = density of the incident DM particle (determined from estimates), m_N = mass of nucleus, v = velocity of DM particle, σ = scattering cross section of the nucleus, E_R = the recoil energy of the collision, and the bracketed term will be averaged over the spread of incoming DM particle velocities.

Since $n_\chi = \frac{p_\chi}{m_\chi}$ (an expansion of the DM particle density), and the scattering cross-section is a measure of probability that scattering will take place in the collision between the nucleus and the DM particle, then the equation can be rewritten as the integral below

$$\frac{dR}{dE_R} = \frac{p_\chi}{m_\chi m_N}\int_{v_{min}}^{v_{max}} d^3 v \cdot v \cdot \tilde{f}(\mathbf{v},t) \cdot \frac{d\sigma}{dE_R},$$

where v_{min} = minimum incident velocity required for the nucleus to scatter, v_{max} = escape velocity ($v_{esc} \approx 544$ km/s through experimental methods), and $\tilde{f}(\mathbf{v},t)$ = DM particle velocity probability distribution in the lab frame.

4.2.1 REFERENCE FRAME TRANSFORMATION

However, since DM velocity distributions calculated as per the Standard Halo Model (a model defining the most widely assumed structure/shape of dark matter distribution across galaxies) are in the Galactic frame of reference, a Galilean boost must be applied to obtain the velocity distributions in a lab frame of reference (as this is what applies to the experiments taking place on Earth). A Galilean boost will transform between coordinates of two reference frames which adhere the constructs of Newtonian physics and differ only by constant relative motion, and hence can be used in this case, to obtain a lab-frame distribution from a Galactic-frame distribution. Therefore:

$$\tilde{f}v = f\big(\mathbf{v} + \mathbf{v}_{obs}(t)\big)$$

$$where\ \mathbf{v}_{obs}(t) = \mathbf{v}_{\odot} + \mathbf{V}_{\oplus}(t),$$

and $\mathbf{v}_{\odot}$ is the velocity of the Sun relative to the desired reference frame ($\mathbf{v}_{\odot} \sim 220 km/s$), while $\mathbf{v}_{\oplus}$ is the velocity of the Earth around the Sun ($\mathbf{v}_{\oplus} \sim 30 km/s$).

The Taylor expansion of velocity distribution is as follows:

$$f\big(\mathbf{v} + \mathbf{v}_{obs}(t)\big) \simeq f\big(\mathbf{v} + \mathbf{v}_{\odot}\big)$$
$$+ \epsilon \cos[\omega(t - t_0)]f'\big(\mathbf{v} + \mathbf{v}_{\odot}\big) + \ldots$$

and the rate equation now can be written as:

$$\frac{dR}{dE_{nr}} = A_0 + A_1 \cos\left[\omega(t - t_0)\right] + \ldots$$

The first term (A0) represents the constant term for the unmodulated rate, and the second term (A1) represents the constant term for the annual modulation of the signal. Further terms are not necessarily relevant outside of cases where DM particles are extremely light, and these constants/expansions of $\tilde{f}(\mathbf{v}, t)$ will be used to simplify the rate equation later.

4.2.2 VELOCITY LIMITS

The next step to calculation involves determining the value of the limits v_{min} and v_{max}. The escape velocity v_{max} has already been approximated experimentally but deriving the value of v_{min} requires reference to the kinematics of the scattering event.

Before delving into this derivation, it is important to define a key constituent of special-relativity kinematics: the 4-dimensional energy-momentum vector, written as A^μ for an arbitrary particle A.

The energy-momentum vector of a particle contains 4 parameters, its energy (E), its momentum in the x direction (p_x), its momentum in the y direction (p_y), and its momentum in the z direction (p_z). Hence, for an arbitrary particle A:

$$A^\mu = \big(E, p_x, p_y, p_z\big) \; where \; \mu = \{0, 1, 2, 3, \}$$

The energy-momentum vector is also useful in special-relativity kinematics because it defines an invariant quantity across all frames of reference: $A \cdot A$

$$A \cdot A = (A_0)^2 - (A_1)^2 - (A_2)^2 - (A_3)^2$$
$$A \cdot A = (E)^2 - (p_x)^2 - (p_y)^2 - (p_z)^2$$

Now, let us consider the collision depicted below in Figure 8, where a DM particle (χ) with momentum k collides with a stationary nucleus N with momentum p. After the collision,

the deflected DM particle (χ') has been deflected along angle $\emptyset$ from the horizontal with momentum p'
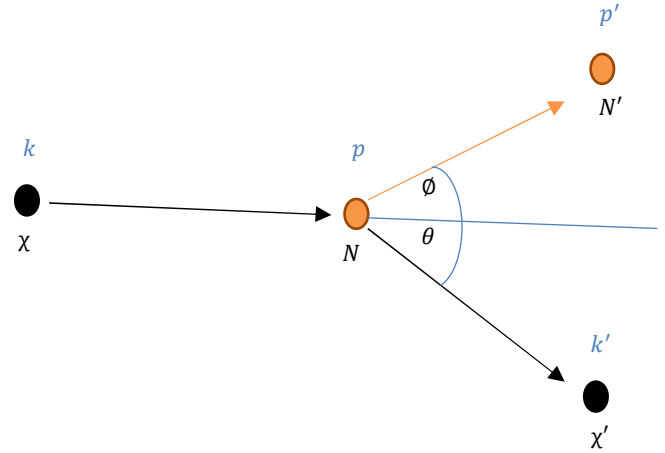

Fig. 8. A basic collision diagram of an incident DM particle colliding with a stationary nucleus

From the diagram, the energy-momentum vector of the initial DM particle χ, with a mass m_χ, momentum k, and velocity v, would be:

$$k^\mu = \left(m_\chi + \frac{1}{2}m_\chi v^2, \; m_\chi v, \; 0, \; 0\right)$$

Similarly, the energy-momentum vector of the initially stationary nucleus N, momentum p, and velocity of 0 would be:

$$p^\mu = (m_N, \; 0, \; 0, \; 0)$$

Now, since momentum is always conserved, and total momentum before the collision must be equal to total after the collision, it may be asserted that:

$$p + k = p' + k'$$

For subsequent calculations, it is more convenient to use newly defined quantitites for momentum transfer (q), and total momentum (P).

$$\therefore \; q = mv \; so \; q = p' - p$$
$$P = p' + p$$
$$P = q + 2p$$

Furthermore, as established earlier:

$$E_R = \frac{q^2}{2m_N}$$

where q = momentum transfer. A simple rearrangement of this equation leaves us with an expression for the momentum as follows:

$$q = \sqrt{2m_N E_R}$$

This expression can now be resolved into its constituent horizontal and vertical components as per the diagram below, ready to be substituted into an energy-momentum vector.

$$q_y = q\sin\theta = \sqrt{2m_N E_R}\sin\theta$$

$$q_x = q\cos\theta = \sqrt{2m_N E_R}\cos\theta$$
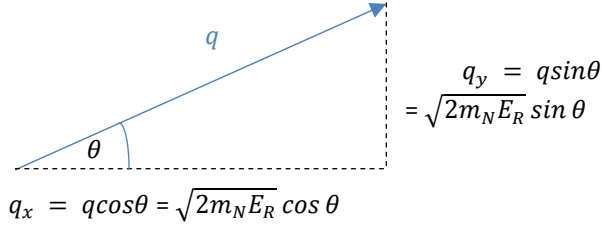
$$\therefore q^\mu = \left(E_R, \sqrt{2m_N E_R}\cos\theta, \sqrt{2m_N E_R}\sin\theta, 0\right)$$

Next, considering the quantity:

$$q \cdot (k - p) - q^2$$

The above expression takes the form of the vector equation below, after correct substitution and rearrangement.

$$= \begin{pmatrix} E_R \\ p_R\cos\theta \\ p_R\sin\theta \\ 0 \end{pmatrix} \cdot \begin{pmatrix} m_\chi + kE_\chi - m_N \\ p_\chi \\ 0 \\ 0 \end{pmatrix} - \begin{pmatrix} E_R \\ p_R\cos\theta \\ p_R\sin\theta \\ 0 \end{pmatrix}^2$$

$$= E_R(m_\chi + k_\chi - m_N) - E_R{}^2 + p_R{}^2 - p_R p_\chi \cos\theta$$

Then, since $p_R{}^2 = 2m_N E_R$

$$= E_R(m_\chi + m_N) - m_\chi v\sqrt{2m_N E_R}\cos\theta = -m_\chi \partial$$

This can be further rearranged to give an expression for $v\cos\theta$ as below:

$$\therefore v\cos\theta = \frac{1}{\sqrt{2m_N E_R}}\left|\frac{E_R(m_\chi + m_N)}{m_\chi} + \delta\right|$$

From the initial diagram of the DM particle and nucleus collision, we can deduce that the minimum value of v, where all kinetic energy from the DM particle is transferred to the nucleus, will occur when θ and $\emptyset = 0$

$$\therefore \cos\theta = 1$$

$$\therefore v_{min} = \frac{1}{\sqrt{2m_N E_R}}\left|\frac{E_R(m_\chi + m_N)}{m_\chi} + \delta\right|$$

In elastic scatterings such as the ones under consideration: $\delta = 0$,

$$\therefore v_{min} = \frac{E_R(m_\chi + m_N)}{m_\chi \sqrt{2m_N E_R}}$$

4.2.3 FINAL INTEGRAL

The initial rate equation is in the form as below:

$$\frac{dR}{dE_R} = \frac{p_\chi}{m_\chi m_N}\int_{v_{min}}^{v_{max}} d^3 v \cdot v \cdot \tilde{f}(\mathbf{v}, t) \cdot \frac{d\sigma}{dE_R}$$

It may be assumed as per the Standard Halo Model that

$$\frac{d\sigma}{dE_R} \propto \frac{1}{v^2}$$

$$\therefore \frac{dR}{dE_R} \propto \int_{v_{min}}^{v_{max}} d^3 v \cdot \frac{f(v + v_\odot)}{v}$$

As mentioned earlier:

$$f(v + v_\odot) = \tilde{f}$$

Therefore, the following term may be generated using the Maxwell-Boltzmann curve as an approximation for incident DM velocity distributions.

$$\tilde{f} \sim e^{\frac{-v^2}{v_0{}^2}}$$

Substitution and rearrangement of the above result, as well as earlier calculated Taylor expansion terms, results in the following simplification of our original rate equation, which can then be graphed and integrated to evaluate scattering rates:

$$\frac{dR}{dE_R} \propto \int_{v_{min}}^{v_{max}} d^3 v \cdot \frac{1}{v} \cdot e^{\frac{-v^2}{v_0{}^2}}$$

$$\frac{dR}{dE_R} \propto \frac{1}{v} \cdot \int_{v_{min}}^{v_{max}} d^3 v \cdot e^{\frac{-v^2}{v_0{}^2}}$$

$$\therefore \frac{dR}{dE_R} \propto \frac{1}{v} \cdot \int_{\frac{E_R(m_\chi + m_N)}{m_\chi\sqrt{2m_N E_R}}}^{v_{max}} d^3 v \cdot e^{\frac{-v^2}{v_0{}^2}}$$

5.1 DIFFERENTIAL ENERGY SPECTRUM PLOT

To begin putting the above calculations into action, below is a differential energy spectrum plot (generated by coding rearrangements of the above calculations in Python) that graphs a range of scattering rates against their respective recoil energies for two different target nuclei – Xenon and Germanium. These two nuclei have specifically been chosen since Xenon represents the target nuclei used by noble-liquid detectors, while germanium represents those used by cryogenic detectors. To keep the graphs consistent with the exploration of WIMPs in direct detection, value uses for DM particle mass $m_\chi \sim 100\ GeV$.
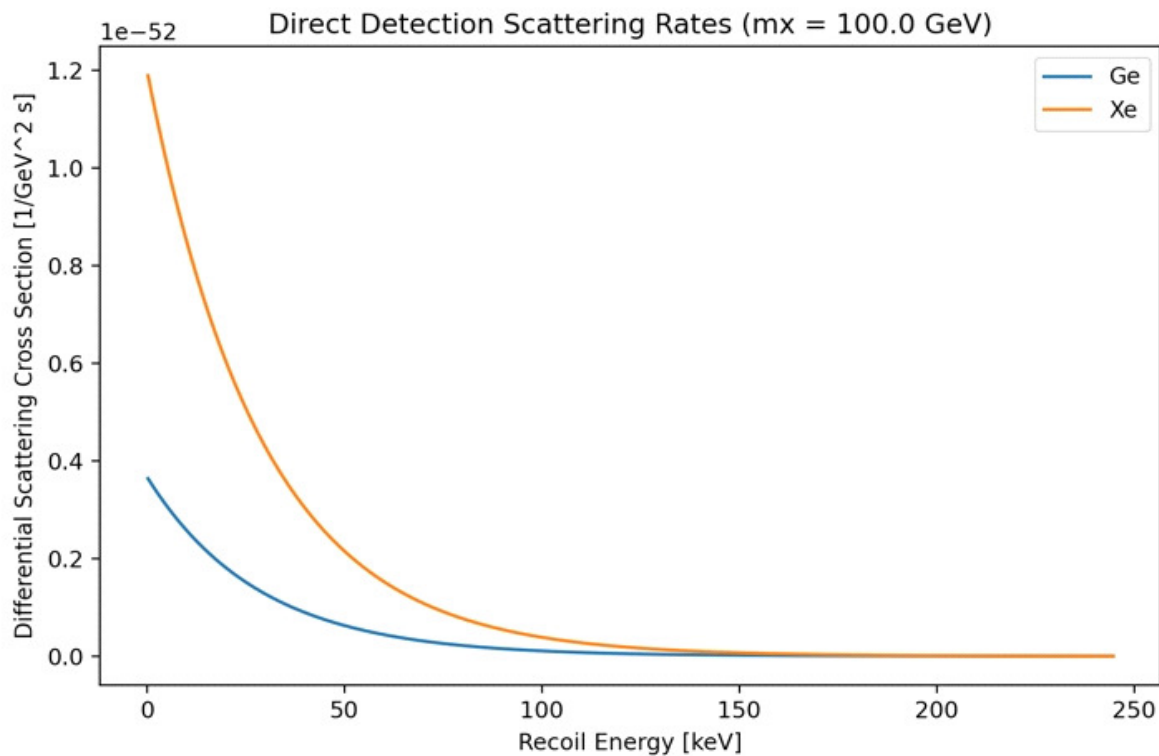

Fig. 9. A plot of differential scattering (scattering rate) against recoil energy of collision

The above graph has been generated by taking numerous different recoil energy values (approximately 1000 different, evenly spaced values between 0 and 100eV), and using the previously determined integral for $\frac{dR}{dE_R}$ (scattering rate/differential scattering) and a form factor calculation to generate respective differential scattering cross sections. The cross-section value used to generate the graph is $10^{-47} cm^2$ (Aprile et. al., 2017)

From this graph, we can see that for increasingly large recoil energies, differential scattering exponentially decreases, and tends to 0 as recoil energies pass thresholds of 150keV. Furthermore, comparisons between liquid noble experiments using Xenon and cryogenic experiments using Germanium can also be made, as differential scattering for the heavier nucleus, Xenon (relative mass number 131.3), is consistently higher than that for the lighter nucleus of Germanium (relative mass number 72.6)

Such graphs could be generated for any target particle. They are useful to forecast potential scattering rates and recoil energies in an experiment, to determine sensible sensitivities, and help distinguish between DM particle interaction scattering, and background electron scattering.

5.2 CODE FOR DIFFERENTIAL ENERGY SPECTRUM PLOT

Pasted below are screenshots of the Python code (briefly explained in commentary) used to generate the plot in Fig. 8.

```python
"""
Description: This code will allow the user to plot a graph of
differential energy spectrum against recoil energy for a specified
target nucleus mass.
Target nucleus masses used here are Germanium and Xenon (CDMS and LUX experiments respectively)
"""


import numpy as np
import matplotlib.pyplot as plt

# 1. Specifying constants and values

# Natural units constants
c = 300000 # km/s
hbar = 1.055*(10**(-34)) # Js

rho_x =  0.4 # Dark matter density - GeV/ c^2*cm^3
v0 = 230/c # Dark matter velocity
vesc = 600/c # Escape velocity
mx = 100*(10**9) # Dark matter mass eV, can go up to 10 TeV
mGe = 6.765*(10**(10)) # mass of germanium (eV)
AGe = 72.63 # Atomic number of germanium (protons + neutrons)
mXe = 1.223*(10**11) # mass of Xenon (eV)
AXe = 131.293 # Atomic number of Xenon
E0 = 0.5*mx*(v0**2) # Average dark matter kinetic energy (eV)
max_Er = 0.5*mXe*(vesc**2) # eV: Enter the max recoil energy value here. You can make it ~ target nucleus mass
cross_section = 10**(-47)   # cm^2, estimate from Fig 5 in Dark Matter Search Results...XENON (Aprile,E.)


recoil_energies = np.linspace(0,max_Er,1000) # List of all recoil energies that will be plotted


def form_factor(mt,Er,A):
    """
    This function takes in the target nucleus mass and the recoil energy.
    It returns the value of the form factor
    """
    q = np.sqrt(2 * mt/(10**9) * Er/(10**9) /(0.197**2))
    a = 0.52
    s = 0.9
    C = 1.23*(A**(1.0/3)) - 0.60
    rn = np.sqrt(C**2 + (7.0/3)*(np.pi *a)**2 - 5*s**2)
    F = 3*np.exp(-(q*s)**2/2)*(np.sin(q*rn) - q*rn*np.cos(q*rn))/ (q*rn)**3
    print(q,a,s,C,rn,F)
    return F

print(form_factor(mXe,E0,AXe))
print()

def differential_scatter_values(mx, mt, Er, A):
    """
    This function takes in the dark matter mass, target nucleus mass and recoil
    energy values and returns a list of diff. scattering values
    mx: dark matter mass
    mt: target nucleus mass
    Er: recoil energy
    A: Atomic mass number of target nucleus
    """
    F = form_factor(mt,Er,A)
    r = 4*mx*mt/ (mx + mt)**2
    f = (cross_section*np.pi/(F**2))**(1/2)
    values = 4*rho_x/((mx/(10**9))*v0*c*100000*np.pi) * (A*F)**2 * f**2 * np.exp(-Er/(r*E0))
    return values


# Plotting steps
plt.plot(recoil_energies/1000,differential_scatter_values(mx,mGe,recoil_energies,AGe),label="Ge")
plt.plot(recoil_energies/1000,differential_scatter_values(mx,mXe,recoil_energies,AXe),label="Xe")
plt.xlabel("Recoil Energy [keV]")
plt.ylabel("Differential Scattering Cross Section [1/GeV^2 s]")
plt.title("Direct Detection Scattering Rates (mx = " + str(mx/(10**9)) + " GeV)")
plt.legend()
plt.show()
```

BIBLIOGRAPHY

[1] Akerib, D. S. *et al.* (2012) 'The Large Underground Xenon (LUX) Experiment'. Available at https://arxiv.org/pdf/1211.3788.pdf (Accessed 20th August)

[2] Aprile, E. *et al.* (2011) 'The XENON100 Dark Matter Experiment', *Astroparticle Physics*, 35(9), pp. 573–590. doi: 10.1016/j.astropartphys.2012.01.003.

[3] Angus, G. W. *et al.* (2013) 'Cosmological simulations in MOND: the cluster scale halo mass function with light sterile neutrinos', *Monthly Notices of the Royal Astronomical Society*, 436(1), pp. 202–211. doi: 10.1093/mnras/stt1564.

[4] Bertone, G., Hooper, D. and Silk, J. (2004) 'Particle Dark Matter: Evidence, Candidates and Constraints', *Physics Reports*, 405(5–6), pp. 279–390. doi: 10.1016/j.physrep.2004.08.031.

[5] Bertone, G. and Merritt, D. (2005) 'Dark Matter Dynamics and Indirect Detection', *Modern Physics Letters A*, 20(14), pp. 1021–1036. doi: 10.1142/S0217732305017391.

[6] Borsanyi, S. *et al.* (no date) *Calculation of the axion mass based on high temperature lattice quantum chromodynamics*.

[7] Carati, A. (2011) 'Gravitational effects of the faraway matter on the rotation curves of spiral galaxies'. Available at: http://arxiv.org/abs/1111.5793 (Accessed: 8 August 2020).

[8] *Dark matter | CERN* (no date). Available at: https://home.cern/science/physics/dark-matter (Accessed: 10 August 2020).

[9] *Five Reasons We Think Dark Matter Exists | by Ethan Siegel | Starts With A Bang! | Medium* (no date). Available at: https://medium.com/starts-with-a-bang/five-reasons-we-think-dark-matter-exists-a122bd606ba8 (Accessed: 8 August 2020).

[10] Gaitskell, R. J. (2004) 'Direct detection of dark matter', *Annual Review of Nuclear and Particle Science*, pp. 315–359. doi: 10.1146/annurev.nucl.54.070103.181244.

[11] Garner, R. (2017) 'Discoveries - Highlights | Shining a Light on Dark Matter'. Available at: http://www.nasa.gov/content/discoveries-highlights-shining-a-light-on-dark-matter (Accessed: 8 August 2020).

[12] Lisanti, M. (2016) 'Lectures on Dark Matter Physics'. World Scientific Pub Co Pte Lt, pp. 399–446. doi: 10.1142/9789813149441_0007.

[13] LUX Collaboration *et al.* (2012) 'Technical Results from the Surface Run of the LUX Dark Matter Experiment', *Astroparticle Physics*, 45, pp. 34–43. doi: 10.1016/j.astropartphys.2013.02.001.

[14] Mirabolfathi, N. (2013) 'Dark Matter Direct Detection With Low Temperature Detectors'. Available at: http://arxiv.org/abs/1308.0044 (Accessed: 8 August 2020).

[15] *Picasso Experiment: Dark Matter* (no date). Available at: http://www.picassoexperiment.ca/dm_neutralino.php (Accessed: 8 August 2020).

[16] Roszkowski, L., Sessolo, E. M. and Trojanowski, S. (2018) *WIMP dark matter candidates and searches-current status and future prospects*.